Scalable and rapid building damage detection after hurricane Ian using causal Bayesian networks and InSAR imagery

Chenguang Wang [a],[1], Yepeng Liu [b],[1], Xiaojian Zhang [b], Xuechun Li [c],
Vladimir Paramygin [b], Peter Sheng [b], Xilei Zhao [b], Susu Xu [c],[*]

[a] *Stony Brook University, 100 Nicolls Road, Stony Brook, 11794, NY, USA*
[b] *University of Florida, 1949 Stadium Road, Gainesville, 32611, FL, USA*
[c] *Johns Hopkins University, 3400 N. Charles Rd, Baltimore, 21218, MD, USA*

ARTICLE INFO

ABSTRACT

Timely and accurate assessment of hurricane-induced building damage is crucial for effective post-hurricane response and recovery efforts. Recently, remote sensing technologies provide large-scale optical or Interferometric Synthetic Aperture Radar (InSAR) imagery data immediately after a disastrous event, which can be readily used to conduct rapid building damage assessment. Compared to optical satellite imageries, the Synthetic Aperture Radar can penetrate cloud cover and provide more complete spatial coverage of damaged zone in various weather conditions. However, these InSAR imageries often contain highly noisy and mixed signals induced by co-occurring or co-located building damage, flood, flood/wind-induced vegetation changes, as well as anthropogenic activities, making it challenging to extract accurate building damage information. In this paper, we introduced a *causality-informed Bayesian network inference* approach for rapid post-hurricane building damage detection from InSAR imagery. This approach encoded complex causal dependencies among wind, flood, building damage, and InSAR imagery using a holistic causal Bayesian network. Based on the causal Bayesian network, we further jointly inferred the large-scale unobserved building damage by fusing the information from InSAR imagery with prior physical models of flood and wind, without the need for ground truth labels. Furthermore, we validated our estimation results in a real-world devastating hurricane—the 2022 Hurricane Ian. We gathered and annotated building damage ground truth data in Lee County, Florida, and compared the introduced method's estimation results with the ground truth and also benchmarked it against state-of-the-art models to assess the effectiveness of our proposed method. The results show that our method advances building damage assessment after hurricanes by accurately reflecting the complex dynamics between wind and flood impacts. Notably, it achieves this without the need for a ground truth label, which is a substantial step forward from traditional methods. Our model registers a 22.6% increase in the Area Under the Curve (AUC) and a 46.29% enhancement in the True Positive Rate (TPR). Moreover, it expedites the detection of building damage, cutting down processing times by up to 83.8%. These improvements mark a considerable leap in efficiency, demonstrating our method's ability to streamline the assessment process markedly over conventional methods.

* Corresponding author.
 E-mail address: sxu83@jhu.edu (S. Xu).
[1] These authors contributed equally to this work.

1. Introduction

Climate change is perpetually intensifying the frequency and severity of extreme weather events, particularly the destructive force of hurricanes, resulting in large-scale infrastructure damage and substantial financial costs. For example, Hurricane Ian in 2022 caused the evacuation of more than 2.5 million people with a loss estimate of 113 billion USD in the United States [1]. In post-hurricane scenarios, immediate information about building damage on a regional scale is critical for effective and timely hurricane response, enabling prioritization of emergency response efforts, saving lives, and providing timely aid, while also informing decisions on allocating funds for reconstruction, revitalizing communities, and enhancing resilience.

Cutting-edge methods for assessing regional building damage after disasters, particularly hurricanes, predominantly rely on sensor-aided inspections (e.g., street-view imagery) and remote sensing using optical imagery. [2–4]. The manual or sensor-aided inspections involve physically surveying affected areas, allowing for detailed observations but often proving time-consuming and resource/labor-intensive for data collection and annotation, limiting its scalability [5–7]. Remote sensing techniques, utilizing aerial or satellite optical imagery [8,9], provide a broad overview of damage on a larger scale, allowing for timely assessments. However, optical imagery quality is highly limited by bad weather conditions (e.g., clouds during hurricanes) and vegetation cover. Furthermore, the majority of present-day optical imagery-based models are plagued by significant negative transfer issues [10]. This term refers to the diminished learning performance observed when a model, initially trained on one context, is applied to a drastically different one. Consequently, these models necessitate comprehensive label annotations from domain experts for fine-tuning when applied to new hurricane events. The process can be inefficient and laborious, particularly when expert input is required to adapt pre-trained models for each new occurrence. The difficulty in acquiring extensive labels makes such approaches difficult to be immediately adopted for near-real-time hurricane responses.

Recently, researchers explore to use the Interferometric Synthetic Aperture Radar (InSAR) imagery, an emerging and powerful technique for measuring surface ground changes caused by natural hazards, for building damage estimation [11,12]. InSAR can penetrate clouds and thus is more robust to bad weather conditions than optical satellite imagery [13,14]. However, InSAR signals are often highly noisy, containing mixed information of surface ground changes jointly induced by multiple hazards, building damage, land cover changes, and anthropogenic activities. For example, building damage may co-occur or co-locate with hurricane-induced hazards (e.g., storm surge and inland flooding), making it challenging to directly attribute changes in InSAR signals to building damage for further building damage assessment. Such co-locating or co-occurring patterns are dominated by underlying highly complex physical causal mechanisms among multiple hazards and building damage. Previous InSAR-based methods mainly built black-box building damage models learned from historical data, but overlooked the mixed signal patterns as well as underlying causal dependencies among multiple hurricane-associated hazards and building damage, thus having limited accuracy.

To address the challenges, we introduce a novel framework, anchored in Bayesian Network principles, to provide rapid and high-resolution estimates of regional building damage by fusing noisy InSAR imagery with physics-based models of hurricane-induced flood and wind, informed by underlying causal dependencies among them. We encode the causal chain of how a hurricane triggers wind and flood, and consequentially jointly causes building damage in a holistic causal graphical model. We further refine this causal graph into a multi-layer hybrid causal Bayesian network for joint inference of unobserved building damage, flood, and wind as well as causal coefficients among them. The major challenges associated with such inference are intractable posteriors of unobserved variables due to their complex multi-layer network structure, unknown causal dependency coefficients, as well as high computational costs for inference over large-scale hurricane zone. In this work, we design a novel inference algorithm based on stochastic variational inference by deriving a tight variational lower bound, composed of unobserved variables posteriors and causal coefficients, to approximate the likelihood of the observed InSAR imagery. With the derived lower bound, we transform the network inference problem into an optimization problem to best approximate the true posteriors and causal dependencies for maximizing the likelihood. With its nature of unsupervised generative learning, this causal Bayesian network can be seamlessly applied across various hurricanes without the need for any ground truth labels.

To validate our framework, we conducted a case study on the 2022 Hurricane Ian, specifically in Lee County, Florida, which was severely damaged during Hurricane Ian. We gathered most of the ground truth data from the street-view imageries collected by Structural Extreme Events Reconnaissance (StEER) Hurricane Ian Response [4]. For regions that were not covered by StEER street-view imagery database, we dispatched four people for a field investigation to conduct surveys of building damage situations for two days. In total, the exterior views of 2472 buildings were collected and their damage levels were labeled. We finally validated the accuracy and timeliness of our framework and compared it with a variety of state-of-the-art methods that use optical satellite imageries and traditional fragility curve-based methods.

In summary, this paper has made multiple significant contributions to the field of rapid post-hazard assessment, advancing the understanding and capabilities in this area through the following contributions:

1. We introduced a novel deep learning model based on the causal Bayesian network, showcasing superior performance in rapid post-disaster assessment, surpassing traditional approaches.
2. Our model uniquely integrates diverse data sources, including environmental factors and remote sensing observations, underpinned by a deep understanding of hurricane damage processes. This integration enhances the model's accuracy and applicability.
3. The model's design, which bypasses the need for ground truth labels, allows for prompt deployment in disaster scenarios. Its ability to handle data noises and uncertainties significantly improves the accuracy of damage assessments.

2. Related work

Accurate and timely post-disaster damage assessment is critical to achieve effective emergency response following a hurricane. Recent advancements in machine learning and imagery technologies have sparked innovation in improving these assessments. Broadly, these approaches can be classified into three categories: methods relying on optical imagery, methods using synthetic aperture radar (SAR) imagery, and conventional fragility models for loss estimation.

Optical Satellite Imagery-based Approaches: In recent years, the utilization of machine learning methods to assess structural damage from optical images has become prevalent, due to the fact that such images are readily available and easy for individuals to comprehend. Various models [3,9,15–23] are presented to analyze images from sources such as satellites, street-view imagery, or aerial vehicles to identify property damage caused by disasters like earthquakes and hurricanes. Khajwal et al. [15] presented a Multi-view Convolution Neural Network (CNN) architecture to evaluate building damage from multiple views using both ground-based images and aerial images. In [3], a coupled disaster damage assessment workflow was proposed, which was based on two CNNs (U-Net [24] and ResNet [25]) for building delineation and multi-degree damage classification. In a study by Calton et al. [9], the transfer learning was applied on ResNet [25], MobileNet [26], and EfficientNet [27] for damage classification and damaged object detection using the optical images from the internet search. Similarly, a key study from Cheng et al. [22], employed a stacked CNNs architecture and trained on the presented in-house visual dataset by adopting the square of earth mover's distance loss over the traditional cross-entropy classification loss function. In another innovative study [23], Cao et al. leveraged CNNs to identify hurricane-damaged buildings. They developed a model that combined the image encoder for processing imagery, fully connected layers for encoding geolocation features, fusion layers for integrating this information, and a class prediction layer for locating damaged structures.

However, the optical image data also poses several challenges, such as sensitivity to atmospheric and weather conditions, difficulty in obtaining high-resolution images, and potential delays in capturing images from satellites. Collecting ground truth data can also be time-consuming and labor-intensive [28]. Additionally, when using optical images for damage assessment, it is necessary to compare pre and post-disaster images [29,30], a process called change detection. This process can be complex due to differences in lighting, angle, and other factors between the pre and post-disaster images. The Siamese neural networks with encoder-decoder architecture were introduced in [29], where two encoders (like ResNet18 [25]) were used to extract the features of pre and post-images separately and one decoder (like U-net [24]) was used to decode those features to do classification.

InSAR Satellite Imagery-based Approaches: InSAR imagery-based methods provide reliable data for damage assessment that is unaffected by visibility constraints, offering a unique perspective in a wide range of applications [31–34]. To be more detailed, Tiampo et al. [35] used Sentinel-1A/B C-band SAR satellite imagery in conjunction with an amplitude thresholding algorithm and DeepLabv3+ (a convolutional neural network) to detect flood extents during Hurricane Harvey. The approach proved particularly effective in identifying floods when applied to SAR GRD data. Similarly, Lin et al. [36] used SAR imagery to detect floods, using a Bayesian probability function to generate a flood probability map. This method revealed an improved performance, especially in urban and vegetated areas. Despite their successes, these methods often struggle to detect cascading secondary hazards and the series of consequential impacts typical of disasters [37]. As such, there is a clear need for further research to develop innovative methods for accurately and efficiently assessing both primary and secondary disaster impacts—an area our study aims to address.

Fragility curves: Conventional methods such as fragility models also contribute to hurricane damage assessment [38–40]. A study by Masoomi et al. [5] proposed a method to predict multi-hazard damage in buildings resulting from hurricanes. They considered multiple effects, including storm surge, waves, and wind, and evaluated the performance of both elevated and non-elevated buildings during Hurricane Ike. While providing detailed estimations, these methods heavily rely on complex, large-scale simulations (which may take weeks or even months to obtain reliable results) and predefined building types (which may not be readily available to the modelers). Therefore, they are more suitable for post-disaster analyses rather than immediate response.

Bayesian Network: Recent advancements in Bayesian Networks (BNs) and probabilistic models have predominantly focused on social sustainability, industrial safety and urban infrastructure [41–43], yet there remains a significant gap in their application to natural disaster scenarios, particularly hurricanes [44]. Amin et al. [45] demonstrated the utility of BNs in dynamic risk assessment within chemical engineering, emphasizing fault detection and risk dynamics. Daley et al. [46] extended BNs' application to process safety analysis in industrial settings, highlighting the importance of integrating diverse data types for more accurate safety predictions. In the realm of urban flooding, Dong et al. [47] explored cascading failure risks and their impacts on infrastructure using BNs, while Joo et al. [48] combined hydrological data with probabilistic modeling in their flood risk assessment using BNs. Xin et al. [49] introduce an approach for integrating hazard scenarios into the Bayesian network model, facilitating the identification of hazards in real time. Wu et al. [50] merge the Bayesian Network model with a geographic information system to evaluate flood disaster risk. Chen et al. [51] present a combined methodology that merges cloud modeling with Bayesian networks to predict earthquake-induced building damages under uncertain conditions. However, the specific challenges of hurricane-induced building damage have not been adequately addressed in these studies. Our research bridges this gap by developing a BN-based framework specifically tailored for post-hurricane building damage estimation. This framework leverages the proven strengths of BNs in capturing complex dependencies, aiming to enhance disaster management strategies and provide tailored responses to the heightened severity of hurricanes in the era of climate change.

3. Method

In this section, we unveil our introduced Bayesian Network-based framework for post-hurricane multi-hazard estimation. We will illustrate how this probabilistic graphical model enhances hazard prediction accuracy by capturing inter-dependencies between risk factors. We will explore the workflow, delve into the methodology, and discuss the strategies we implemented to boost efficiency. This approach aims to revolutionize hazard estimation post-hurricane, aiding effective disaster management.
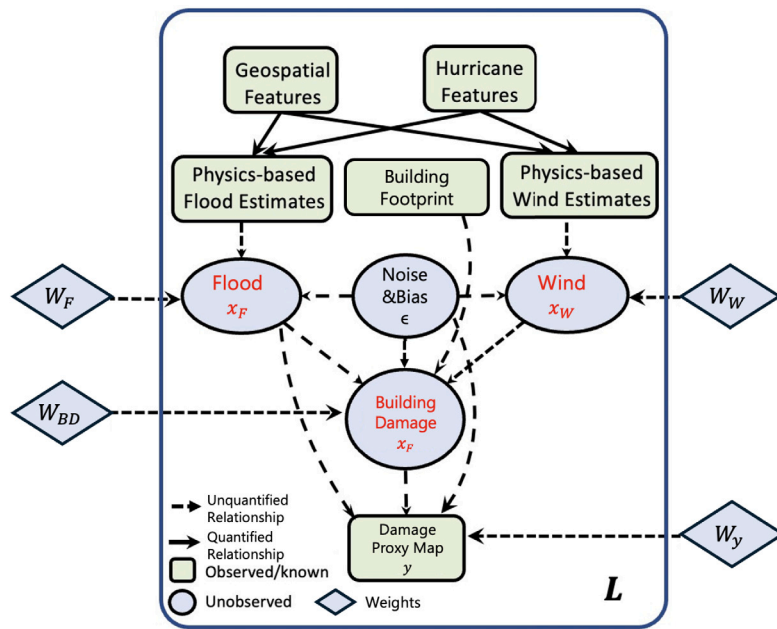
Fig. 1. Causal Bayesian network that depicts causal dependencies among hurricane-induced wind and flood, building damage, Damage proxy maps (DPMs), and environmental noises. L refers to the number of locations/pixels within the target area. The posterior probability of, and at each location are the objectives that our system estimates. Green boxes refer to the variables that have data constraints. Blue circles refer to nodes that are not observed or unknown. Blue diamonds are the causal coefficients, which are unknown, that quantify the causal effects of parent nodes on hurricane-induced flood, hurricane-induced wind, building damage, and DPMs. Solid lines indicate quantified relationships in the Bayesian network and dashed lines indicate unquantified relationships between the input and nodes. For each pixel or location, we construct a Bayesian network. We optimize the variational lower bound, as derived in Eq. (12), to approximate the true posteriors of the unobserved variables. Meanwhile, we optimize the parameters/coefficients that quantify the causal relationships among known and unknown variables. The detailed descriptions and equations related to these procedures are provided in Section 3.

3.1. Causal Bayesian network formulation for Hurricane damage chain

A hurricane can potentially trigger a multitude of cascading hazards, and it becomes crucial to understand which of these hazards significantly impact the integrity of buildings. To accurately infer building damage state from noisy InSAR imagery products like the foundation of this process, which centers around the DPMs, begins with Synthetic Aperture Radar (SAR), a technology that employs radar signals to image the Earth's surface [52] Subsequently, Interferometric Synthetic Aperture Radar (InSAR) comes into play, building upon SAR's capabilities by comparing images to detect subtle surface variations, particularly in elevation and ground deformation [52]. These technologies are crucial in developing DPMs, which quantify the impact of disasters by analyzing shifts in radar signal properties [53], indicative of alterations in infrastructure and the environment. The role and methodology of DPMs in mapping the effects of Hurricane Ian are elaborated in Section 4.3.

As shown in Fig. 1. our network delineates the causal interdependencies among key variables such as hurricanes, floods, wind, building damage, and DPMs, alongside environmental noises and biases, with each type of node and edge meticulously representing distinct aspects of the system. Green rectangle nodes embody known variables, such as physics-based wind/flood estimates, building footprints, and DPMs, serving as the foundational elements, which are detailed in Section 3.1.1. Notably, Geospatial Features and Hurricane Features here encompass critical parameters for physics-based wind and flood estimation methods, including wind speed, wave heights, and sea level. Moreover, the network is designed to leverage these known nodes and the causal relationships to infer the damage of unknown variables, denoted by the Blue circle, particularly flooding, wind, and building damage.

Furthermore, it endeavors to quantify the causal coefficients that define the interaction strength and direction between these elements. Solid lines between nodes indicate direct, known causal relationships based on prior knowledge, while dashed lines represent inferred causal relationships, deduced through analysis and modeling. Each edge within this graphical representation is not just a conduit for data flow but a crucial indicator of causality, illustrating how variables like hurricane intensity can directly influence subsequent phenomena such as flood levels or structural integrity, thus providing a comprehensive framework for inferring the interdependencies among these nodes. Besides, our stochastic variational inference method enables us to approximate the causal coefficients and posteriors of unobserved variables—such as flooding, wind, and building damage—across each location or pixel, denoted by 'L'. Consequently, the graph is designed to provide probabilities for intermediate hazards and impacts at the granular level of high-resolution grid cells, through the strategic integration of physical models and DPMs.

Building on this objective, two key aspects of our approach are to accurately model the node presented in Fig. 1 and transform the conceptual graph into a probabilistic graphical model. We began by defining the attributes of nodes within our causal graph,

grounding these definitions in empirical knowledge. For the nodes representing wind and flood, we estimate wind speeds using time-series data from monitoring stations [54] and maximum flood depths through a combination of flood sensing data and coastal-wave modeling [55], a method supported by prior research [56,57]. However, the simplified physical models and sparse sensing data, might not capture the complex evolving conditions of a hurricane and thus may result in highly biased spatio-temporal wind speed and flood depth estimates, which is a common challenge in existing practice [58,59]. Thus, in this study, we integrate the post-hurricane large-scale observations from InSAR imagery with the inaccurate wind/flood estimates to enhance damage assessment accuracy. The InSAR data provides high-resolution imagery that records pre- and post-hurricane changes in building damage and landscape, alongside environmental noise. We employ a causal graph model that utilizes the causal dependencies among wind, flood, building damage, environmental noises, and InSAR observations, for accurate damage evaluation.

Subsequently, we progress to converting the conceptual causal graph into a probabilistic graphical model. These parameters are translated into conditional probability distributions, fine-tuned with data from wind and flood measurements we defined previously. Such distributions capture the variable nature of these elements, helping us build Bayesian networks based on them. Our model also integrates InSAR-derived DPM data with the binary variable for the location height change. Then, Within this framework, we define the conditional dependencies that dictate the relationships and interactions between physical phenomena like wind and flood and their consequent effects on building damage, streamlining the complex interdependencies into an analyzable model. Afterward, we utilize a stochastic coordinate descent method to fine-tune the coefficients depicting causal links among predictors, aiming to maximize the marginal likelihood of observed DPMs based on prior physical models. This ensures an optimal representation of causal coefficients and unobserved variables' posteriors. Built on this causal graphical framework, our system calculates the probabilities of various hazards and their impacts at high-resolution grid cells, using empirical models and DPM data.

This integration of remote sensing data with the physical parameters of hazards enables the Bayesian network to precisely delineate the relationships between nodes and calculate the probabilities of building damage. In post-disaster scenarios, access to detailed building characteristics (such as types, structures, first-story heights, repair records, materials, and land use plans) is severely limited due to a lack of data inventory, vast number of buildings, and urgent needs of rapid assessments [60–63]. Therefore, our study assumes that we have no access to detailed building characteristics data. Instead, InSAR imagery products directly capture the building deformation information from satellites, although highly noisy, making it possible to assess building damage even without detailed structural characteristics. To extract accurate building damage state from noisy InSAR data, we utilize causal relationships to combine building deformation information (InSAR data) with the impacts of hurricane-induced wind and flooding (Physical model). This enables accurate building damage assessments, bypassing the need for detailed structural characteristics.

3.1.1. Node variables modeling

We identify our feature vertices, also known as unobserved variables, which include Flood and Wind, denoted as x_F and x_W respectively. As per the findings of previous research [5,64], these variables are considered continuous and assumed to follow a lognormal distribution.

We also define Building Damage as x_{BD}, assuming it is a binary variable where 1 represents severe damage or complete destruction, and 0 signifies no damage or minor damage. Each unobserved variable in X is denoted as x_i, with i being an element of the set $\{W, F, BD\}$. For every x_i, the set $\mathcal{P}(i)$ contains its parent nodes. As illustrated in Fig. 1, the set of parent nodes is predetermined based on our understanding of the physical causal chain. Furthermore, we incorporate wind and flood estimates, denoted as a_W for wind and a_F for flooding, derived from physics-based models that utilize geospatial and hurricane features.

The parent nodes of any sensed observations X are represented by $\mathcal{P}(x)$. A leak node, denoted as $x_{0i} = 1$, is included that remains consistently active, thus ensuring the possibility of child node activity even when other parent nodes are inactive.

The Disaster Proxy Map(DPM) directly represents the impact of multi-hazard events. The Interferometric Synthetic Aperture Radar (InSAR) on the satellite can capture detailed height changes for a specific location, denoted as $y > 0$ in the DPMs. Furthermore, we assume there exist environmental noises for each unobserved hazard and building damage, namely ϵ_y and $\epsilon_i, i \in \{W, F, BD\}$, following a standard normal distribution.

3.1.2. Causal dependency modeling

After establishing variable representation, it becomes crucial to parameterize their dependencies (i.e., edges between nodes). We denote $w_{ji} (j \in \mathcal{P}(i))$ as the weight of each parent node's impacts on the child node. Take the node of Flood as an example, the set of weights for Flood w_F, denoted as blue diamonds in Fig. 1, contains all weights that parameterize the causality from its parents, including from the prior model to flood ($w_a F$), from noises to flood (w_{ϵ_F}), from bias to flood ($w_0 F$). Based on these considerations, we have articulated the causal dependencies as follows::

Given the DPM y, we assume that the causal dependencies from parents $\mathcal{P}(y)$ to y is lognormal (LN):

$$\log y = \sum_{k \in \mathcal{P}(y)} w_{ky} x_k + w_{\epsilon_y} \epsilon_y + w_{0y} \tag{1}$$

As illustrated in Fig. 1, the parent nodes of InSAR observation include flood, building damage, environmental noises, as well as the leaky node, i.e. $\mathcal{P}(y) = \{x_F, x_{BD}, \epsilon_y, x_0\}$.

For unobserved variables such as wind and flood, i.e., $i \in \{W, F\}$, their parent nodes include physics-based wind/flood model estimates (a_i), environmental noises ϵ_i and leaky node x_0. Similarly, given our assumption that the continuous variables x_F and x_W follow a lognormal distribution, we formulate the causal dependencies from the parent nodes $\mathcal{P}(i)$ to its child nodes x_i as

$$\log x_i = \sum_{k \in \mathcal{P}(i)} w_{ki} x_k + w_{\epsilon_i} \epsilon_i + w_{0i} \tag{2}$$

For building damage $i = BD$, $\mathcal{P}(BD) = \{x_F, x_W\}$, as depicted in Fig. 1. As we defined in Section 3.1.1, x_{BD}, i.e. building damage, is a binary variable. Consequently, we formulate the causal dependencies from the parent nodes $\mathcal{P}(BD)$ to the child node x_{BD} as

$$\log \frac{p(x_i = 1|\mathcal{P}(i), \epsilon_i)}{1 - p(x_i = 1|\mathcal{P}(i), \epsilon_i)} = \sum_{k \in \mathcal{P}(i)} w_{k,i} x_k + w_{\epsilon_i} \epsilon_i + w_{0i}. \tag{3}$$

It can be seen that all unquantified causal dependencies represented by dashed arrows in Fig. 1 are all formulated into mathematical equations, together with the unobserved variables represented by blue circles. It is thus challenging to infer this multi-layer Bayesian network with a mixture of unknown continuous variables, unknown discrete variables, as well as unknown dependency parameters.

3.2. Stochastic variational inference

Once the Bayesian network is established, the next step is to jointly infer the posterior of unobserved building damage and secondary hazards. However, this presents a unique challenge as both the causal dependency parameters and the distributions of secondary hazards and building damage remain unknown. Further complicating the situation, the target affected area may be expansive, making it computationally burdensome to conduct joint inference over large-scale high-resolution maps (e.g., InSAR imagery for Hurricane Ian contains 2000*3000 pixels).

To address this issue, we employ variational inference, which allows us to first factorize the Bayesian network and then approximate the posterior distributions of the unobserved variables by maximizing the log-likelihood of the observed variables. Importantly, to ensure the scalability of our method, the variational inference is implemented on a small, randomly sampled batch of locations during each iteration. This approach facilitates a balance between computational efficiency and the comprehensive analysis of large areas. Incorporating the concept of variational inference, the central notion is to derive and maximize a tight lower bound on the log-likelihood of sensing observations. This lower bound is frequently expressed as a function of the posteriors of unobserved variables (denoted as q) and weights, symbolizing the causal dependencies (w). This approach plays a vital role in transforming our understanding of the inter-dependencies within the network and presents a structured, efficient way of approximating the posterior distributions. Therefore, the derivation of variational lower bound is :

$$\log p(Y) = \sum_{l \in N} \log \int p(y^l, X^l, \epsilon^l) d(X^l, \epsilon^l)$$
$$\geq \sum_{l \in N} \int q(X^l, \epsilon^l) \log \frac{p(y^l, X^l, \epsilon^l)}{q(X^l, \epsilon^l)} d(X^l, \epsilon^l) \tag{4}$$
$$= \sum_{l \in N} \{ \underbrace{\mathbb{E}_{q(X^l, \epsilon^l)}[\log p(y^l, X^l, \epsilon^l)]}_{[1]} - \underbrace{\mathbb{E}_{q(X^l, \epsilon^l)}[\log q(X^l, \epsilon^l)]}_{[2]} \}$$

where q is the posteriors of all unknown variables.

To further obtain the explicit form of the final variational bound, we expand the **item [1]** as:

$$\mathbb{E}_{q(X^l, \epsilon^l)}[\log p(y^l, X^l, \epsilon^l)] = \underbrace{\mathbb{E}[\log p(y|\mathcal{P}(y), \epsilon_y)]}_{[3]} + \underbrace{\sum_i \mathbb{E}[\log p(x_i|\epsilon_i, \mathcal{P}(i))]}_{[4]} + \underbrace{\sum_i \mathbb{E}[\log p(\epsilon_i)] + \mathbb{E}[\log p(\epsilon_y)]}_{C_1} \tag{5}$$

Since $y|\mathcal{P}(y) \sim LN(\sum_{k \in \mathcal{P}(y)} w_{ky} x_k + w_{0y}, w_{\epsilon_y}^2)$, where $\mathcal{P}(y) = \{F, BD\}$. So we can calculate **item [3]**:

$$\mathbb{E}[\log p(y|\mathcal{P}(y), \epsilon_y)] = -\log y - \log |w_{\epsilon_y}| - \frac{(\log y)^2 + w_{0y}^2 - 2w_{0y} \log y}{2w_{\epsilon_y}^2}$$
$$+ \frac{\sum_{k \in \mathcal{P}(y)} w_{ky}^2 \mathbb{E}(x_k^2) + 2(w_{0y} - \log y) \sum_{k \in \mathcal{P}(y)} w_{ky} \mathbb{E}(x_k)}{2w_{\epsilon_y}^2} \tag{6}$$

where $k = F$: $E(x_k) = \exp(\mu_k + \sigma^2/2)$ and $E(x_k^2) = (\exp(\sigma^2) - 1)\exp(2\mu_k + \sigma^2) + \exp(\sigma^2 + 2\mu_k)$. ; For $k = BD$, $\mathbb{E}(x_i) = q_k, \mathbb{E}(x_i^2) = q_k$. For the **item [4]**, It should be derived separately because the $i \in \{W, F\}$ and $i \in \{SD, RD\}$ are different situations here, so the equation could be expanded first into: $\sum_i \mathbb{E}[\log p(x_i|\epsilon_i, \mathcal{P}(i))] = \sum_{i \in \{W,F\}} \mathbb{E}[\log p(x_i|\epsilon_i, \mathcal{P}(i))] + \sum_{i \in \{RD,BD\}} \mathbb{E}[\log p(x_i|\epsilon_i, \mathcal{P}(i))]$ Then based on this equation, we could divide the equation into 2 different scenarios. When the unobserved variable is continuous, we will derive the $\mathbb{E}[\log p(x_i|\epsilon_i, \mathcal{P}(i))]$ for $i \in \{W, F\}$. Since $x_i|\epsilon_i$ follows a lognormal distribution, then $\log x_i|\epsilon_i$ follows a normal distribution. Then we could get the **item [4]** for $i \in \{W, F\}$:

$$\mathbb{E}[\log p(x_i|\epsilon_i, \mathcal{P}(i))] = -(w_{a_i} a_i + w_{0i}) - \log |w_{\epsilon_i}| \tag{7}$$

When an unobserved variable i is discrete, for example, a binary distribution, the crux of this computation involves leveraging the activation function to derive the final outcome. It is essential to acknowledge that the computation of log expectation for binary distributions often demands an upper bound for numerical stability. Direct computation may confront precision issues or even become undefined, especially when probabilities approach infinitesimally small or zero values. The introduction of a tight upper

bound assists in circumventing these issues while preserving the model's expressiveness. Guided by this principle, we can determine the result of $\mathbb{E}(\log p(x_i = m_i | \mathcal{P}(i), \epsilon_i))$ for $i \in \{BD\}$. The computation of **item [4]** for $i \in \{BD\}$ is :

$$
\begin{aligned}
\mathbb{E}(\log p(x_i | \mathcal{P}(i), \epsilon_i)) &= q_i \mathbb{E}(-\log[1 + \exp(-w_{\epsilon_i} \epsilon_i - w_{0i} - \sum_{k \in \mathbf{P}(i)} w_{ki} x_k)]) \\
&+ (1 - q_i) \mathbb{E}(-\log[1 + \exp(w_{\epsilon_i} \epsilon_i + w_{0i} + \sum_{k \in \mathbf{P}(i)} w_{ki} x_k)]).
\end{aligned}
\tag{8}
$$

However, the distribution of $-\log[1 + \exp(w_{\epsilon_i} \epsilon_i + w_{0i} + \sum_{k \in \mathbf{P}(i)} w_{ki} x_k)]$ is intractable as it is a log-sum-exp of mixing a series of discrete variables and continuous variables. Therefore, we need to get a tight lower bound of its expectation. Here without the loss of generality, we start from the case where i has a single active parent.

With multivariable Taylor's expansion, we can apply the standard quadratic bound for $\log(1 + \exp)$ [65]:

$$
\log(1 + e^z) \le g(\gamma)(z^2 - \gamma^2) + \frac{z - \gamma}{2} + \log(1 + e^\gamma)
$$

where $\gamma \in (0, \infty)$, $g(\gamma) = \frac{1}{2\gamma}[\frac{1}{1+e^{-\gamma}} - \frac{1}{2}]$. Moreover, with multivariable Taylor's expansion, we will finally obtain the lower bound for $i = BD$ as

$$
\mathbb{E}(\log p(x_i | \mathcal{P}(i), \epsilon_i)) \ge -\sum_{\substack{v_i, v_j \in \{0,1\} \\ j \in \mathbf{P}(i)}} \log\{1 + \exp[(-1)^{v_i} \cdot (w_{0i} + \sum_{j \in \mathbf{P}(i)} I(j, \alpha_i) w_{ji}) \qquad + \frac{w_{\epsilon_i}^2}{2}]\} \prod_{k \in \{i,j\}} (q_k^l)^{v_k} (1 - q_k^l)^{1 - v_k},
\tag{9}
$$

where

$$
I(j, \alpha_i) = \begin{cases} \dfrac{1 - (-1)^{v_j}}{2} & \text{if } j \text{ is unobserved} \\ \alpha_i & \text{if } j = \alpha_i, \end{cases}
$$

$$
\mathbb{E}(\log p(x_i | \mathcal{P}(i), \epsilon_i)) \ge (1 - q_i)\mathbb{E}(z_i) - \{g(\gamma_i)(\mathbb{E}(z_i^2) - \gamma_i^2) + \frac{\mathbb{E}(z) - \gamma_i}{2} + \log(1 + e^{\gamma_i})\}
$$

where

$$
\begin{aligned}
\mathbb{E}(z) &= \sum_{k \in \mathcal{P}(i)} w_{ki} \mathbb{E}(x_k) + w_{0i} \\
\mathbb{E}(z^2) &= \sum_{k \in \mathcal{P}(i)} w_{ki}^2 \mathbb{E}(x_k^2) + w_{\epsilon_i}^2 + w_{0i}^2 + 2w_{0i} \sum_{k \in \mathcal{P}(i)} w_{ki} \mathbb{E}(x_k) + \sum_{\substack{r,s \in \mathcal{P}(i) \\ r \ne s}} w_{ri} w_{si} \mathbb{E}(x_r) \mathbb{E}(x_s)
\end{aligned}
\tag{10}
$$

It is noted that for $k \in \{W, F\}$, as they are leaf nodes with all parent nodes known, and we postulate that x_k follows a lognormal posterior with parameters of μ_k and σ_k, there is $\mathbb{E}(x_k) = \exp(\mu_k + \sigma^2/2)$ and $\mathbb{E}(x_k^2) = (\exp(\sigma^2) - 1)\exp(2\mu_k + \sigma^2) + \exp(\sigma^2 + 2\mu_k)$. After we finish the all the calculation form the **item [1]**, we further move to derive the expansion of the **item [2]** as:

$$
\mathbb{E}_{q(X^l, \epsilon^l)}[\log q(X^l, \epsilon^l)] = \sum_{i \in \{\}} q_i \log q_i + (1 - q_i) \log(1 - q_i) - \sum_{i \in \{F, W\}} [\mu_i + \log \sigma_i] + C_2.
\tag{11}
$$

where C_2 is a fixed constant.

After we all get all the result from the expansion for each items, we could get the final variational lower bound:

$$
\begin{aligned}
\log p(Y) &= \sum_{l \in N} \{\underbrace{\mathbb{E}_{q(X^l, \epsilon^l)}[\log p(y^l, X^l, \epsilon^l)]}_{[1]} - \underbrace{\mathbb{E}_{q(X^l, \epsilon^l)}[\log q(X^l, \epsilon^l)]}_{[2]}\} \\
&= -\log y - \log|w_{\epsilon_y}| - \frac{(\log y)^2 + w_{0y}^2 - 2w_{0y} \log y}{2w_{\epsilon_y}^2} \\
&+ \frac{\sum_{k \in \mathcal{P}(y)} w_{ky}^2 \mathbb{E}(x_k^2) + 2(w_{0y} - \log y) \sum_{k \in \mathcal{P}(y)} w_{ky} \mathbb{E}(x_k)}{2w_{\epsilon_y}^2} \\
&- \sum_{i \in \{W, F\}} (w_{a_i} a_i + w_{0i}) - \log|w_{\epsilon_i}| \\
&+ \sum_{i \in \{RD, SD\}} \{\mathbb{E}(z_{m_i}) - \{\mathbb{E}(\hat{\beta}_i) + \sum_{m_i} g(\gamma_{m_i})[\mathbb{E}(z_{m_i}^2) + \mathbb{E}(\hat{\beta}_i^2) - 2\mathbb{E}(z_{m_i})\mathbb{E}(\hat{\beta}_i)] \\
&- \sum_{m_i} \gamma_{m_i}^2 + \frac{\sum_{m_i} \mathbb{E}(z_{m_i}) - (M_i + 1)\mathbb{E}(\hat{\beta}_i) - \sum_{m_i} \gamma_{m_i}}{2} + \sum_{m_i} \log(1 + e^{\gamma_{m_i}})\}\} \\
&- \sum_{i \in \{SD, RD\}} q_{i, m_i} \log q_{i, m_i} + \sum_{i \in \{F, W\}} [\mu_i + \log \sigma_i]
\end{aligned}
\tag{12}
$$

it is to be noted that detailed derivation is listed in the supplementary file.

With items derived, we finally obtain a tight variational lower bound for the given causal Bayesian network for hurricane-induced hazards and damage estimation. We further proceed to maximize this lower bound to find the optimal combinations of posteriors of

unobserved variables as well as causal coefficients (weights). Given that both the posteriors and weights are unknown, we employ an Expectation–Maximization (EM) approach to achieve this. In the expectation step, we extract closed-form update equations for the posteriors of W, F, and BD by maximizing the lower bound and setting the gradients of the lower bound to 0.

For $k = BD$, we derive closed-form update equations for the local posteriors by maximizing the lower bound and setting the gradients of the lower bound to 0. So we could get the equation:

$$q_k = \exp(\frac{w_{ky}^2 + 2(w_{0y} - \log y)w_{ky}}{2w_{\epsilon_y}^2} - 1) \tag{13}$$

During the maximization step, we apply Stochastic Gradient Descent (SGD) updates to estimate the optimal weights, using a mini-batch of data randomly sampled from various locations. We have tailored Stochastic Variational Inference to expedite the computational process across a large-scale, high-resolution map. Consequently, the edge weights at iteration t + 1 are updated as:

$$\mathbf{w}_{(t+1)} = \mathbf{w}_{(t)} + \rho A \nabla \mathcal{L}(\mathbf{w}) \tag{14}$$

Here, ρ modulates the learning rate, while A serves as a preconditioner. In our case, A is set up as the identity matrix to spur convergence to high likelihood models. At each iteration, we begin by randomly sampling a mini-batch of locations from the given map. Subsequently, we implement the expectation and maximization steps to update the posterior estimations and the global weight parameters. As the model converges, we can estimate the optimal posteriors of wind, flooding, and building damage from the hurricane.

Local pruning strategy for computational efficiency: Given the large map, we further design a local pruning strategy to remove unnecessary nodes in a local causal graph and accelerate the computation. This strategy is motivated by the observation that real-world causal graphs are typically sparse: only a small subset of nodes stay active in a specific location. One example is that a location without any building footprints will not have damaged buildings, i.e., building damage nodes should be inactive. Therefore, we can prune these inactive nodes while keeping the active ones crucial for parameter updates.

4. A case study of Hurricane Ian

The 2022 Hurricane Ian [66] is chosen as the case study. This section introduces the background of Hurricane Ian, and provides a detailed description of street-view imagery data collection, data pre-processing and damage level annotation.

4.1. Background of Hurricane Ian and study site

Hurricane Ian made landfall in Lee County, FL, on September 28, 2022. Lee County, FL, is located in southwest Florida. The population estimate is 822,453 as of 2022. Its county seat is Fort Myers and the largest city is Cape Coral. According to Hurricane Ian Progress Report provided by the government of Lee County,[2] this hurricane strongly affected all 47 miles of beach shoreline and around 35 miles of which were categorized as major erosion. All county beaches and parks were stroked by this storm and more than 130,000 residents were forced to seek housing assistance. The mandatory evacuation order was first issued in Lee County for Evacuation Zone A and B at 09:00 a.m. on September 27, 2022, and then the evacuation orders were extended to Evacuation Zone C in the following hours. The track for Hurricane Ian, the spatial distribution of evacuation zones, and the study site are presented in Fig. 2(a).

4.2. Building damage ground truth collection

We collected street-view imagery data of buildings that were impacted by Hurricane Ian from both the Structural Extreme Events Reconnaissance (StEER) Hurricane Ian Response[3] and our field investigation. The data collection process yields an imagery dataset of 2472 buildings impacted by the hurricane. More details can be found in Appendix.

Damage Level Annotation: We labeled the damage level for each building by following StEER's Field Assessment Structural Team (FAST) handbook [67]. We should note that the damage level annotation is purely based on the exterior (i.e., outside portions of a structure) of each building. The damage level was classified into the following five categories: 0 - No damage or very minor damage, 1 - Minor damage, 2 - Moderate damage, 3 - Severe damage, and 4 - Destroyed. Two annotators were trained and deployed to code the label for each building. A small dataset containing 100 images was randomly sampled from the whole dataset for an inter-coder reliability test. Each annotator coded the damage level independently. We used *Krippendorff's alpha* [68] and correlation coefficient to measure the reliability of the damage level code identified by two annotators. The Krippendorff's alpha was finally calculated as 0.86 and the correlation coefficient of two annotators' damage level annotations was 0.97 and statistically significant at 0.001 level, indicating a highly consistent damage level recognition. After reaching an agreement on all conflicting labels, the remaining images were then split by two annotators. The final dataset includes 1785 buildings coded as level 0 (no damage), 292 as level 1 (minor damage), 244 as level 2 (moderate damage), 119 as level 3 (major damage), and 32 as level 4 (destroyed). An example of the damage level-labeled parcels in a selected community is shown in Fig. 2(b). Most of the buildings are below moderate damage, and only 151 (6.1%) buildings have major damage or are completely destroyed. In total, 72.2% of the sampled parcels have no obvious exterior damage while the remaining 27.8% of which is damaged. More details about the distribution of the damage level across evacuation zones are presented in Table 4 in Appendix.
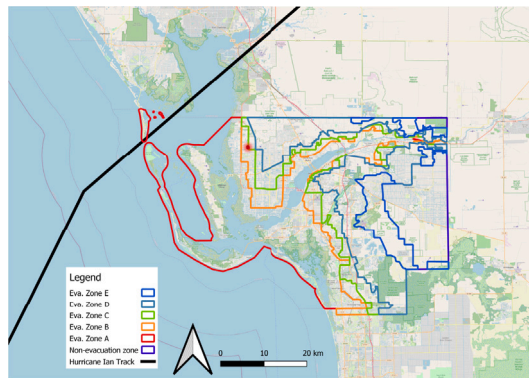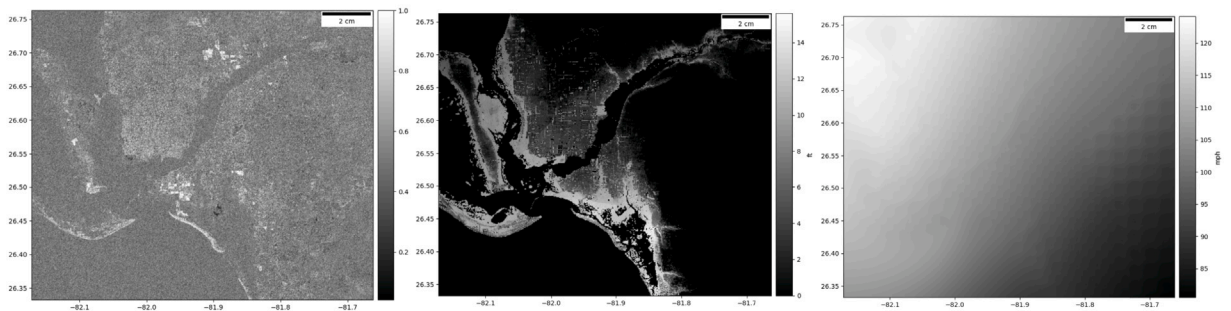

(a) Hurricane Ian Track and Lee County Evacuation Zones
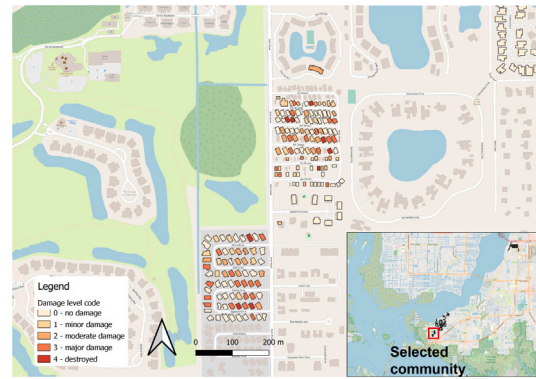
(b) An example of damage level-labeled parcels in a selected community

Fig. 2. Figures of Hurricane Ian Track and damage level-labeled parcels.

Fig. 3. Overview of the DPM, Flood Map and Wind Map in Lee County, FL (from left to right).

4.3. Datasets used in causal Bayesian networks

As shown in Fig. 1, our framework takes wind map, flood map, and damage proxy map(derived from InSAR imagery) as input for inference.

Wind Map and Flood Map: The National Institute of Standards and Technology (NIST), in collaboration with Applied Research Associates, Inc. (ARA),[4] has embarked on a significant project to develop a comprehensive surface-level wind field model for Hurricane Ian in Florida. Utilizing advanced simulation techniques, the team has collated peak and sustained wind data as shown in Fig. 3. This dataset provides unprecedented insight into the hurricane's progression and intensity.

The Flood map is based on the simulation of a coupled storm surge-wave modeling system CH3D-SWAN [69] using boundary-fitted grids with a minimum grid size of 20 meters for the Charlotte, Lee, and Collier Counties of Florida. The model was forced by a hurricane wind model for Ian [70] with offshore water level simulated by a large-scale surge and tide model. More details can be found in Appendix.

Damage Proxy Map: The Damage Proxy Map (DPM), shown as Fig. 3, a multi-temporal coherence-based representation of damage, has been created by the Advanced Rapid Imaging and Analysis (ARIA) team at NASA's Jet Propulsion Laboratory and California Institute of Technology. The map illustrates areas in Florida, USA, that were likely affected by Hurricane Ian in September 2022. The DPM was derived from synthetic aperture radar (SAR) images obtained by the Copernicus Sentinel-1 satellites, operated by the European Space Agency (ESA), from April 5, 2022, to October 2, 2022 [71].

The map encapsulates an area of about 85 by 76 km (53 by 47 miles), centered on Fort Myers, Florida. A large red polygon delineates the boundary of the source data, with each pixel representing an approximately 10-meter square in the primary image. One salient advantage of the DPM, especially when compared to optical images, is its construction via InSAR (Interferometric Synthetic Aperture Radar). InSAR, a technique for mapping ground deformation, utilizes radar images of the Earth's surface collected from orbiting satellites [72]. In contrast to visible or infrared light, radar waves can penetrate most weather clouds and function equally well in darkness, making it possible to track ground deformation even under adverse weather conditions and during nighttime — an invaluable advantage during a hurricane crisis.

---

[4] https://www.nhc.noaa.gov/archive/2022/IAN_graphics.php

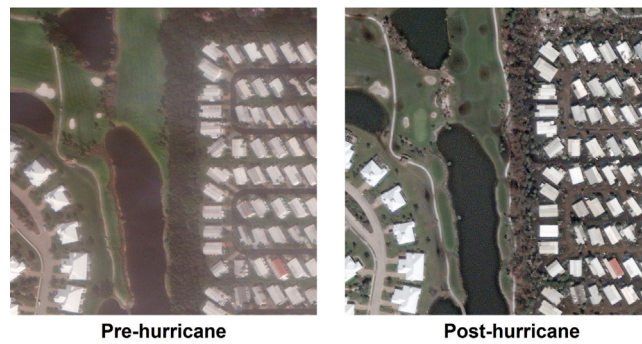**Pre-hurricane**   **Post-hurricane**

Fig. 4. An example of the remote sensing image patch.

In our research context, the DPM is foundational not just because it provides direct visualization of the impacts of multi-hazard events, but also because it supplies the grid system for our rasterization work involving other data sets, such as building footprints, among others.

4.4. Evaluation metrics

In our study, we employ the receiver operating characteristic (ROC) curve and the area under the ROC curve (AUC) as the primary evaluative metrics. The ROC curve is a graph that plots the True Positive Rate (TPR) against the False Positive Rate (FPR). Here, the TPR, representing the likelihood of our model accurately identifying a damage event when the damage has indeed occurred, is plotted on the y-axis. Conversely, the FPR, indicating the probability of the model predicting the occurrence of damage when no damage has happened, is plotted on the x-axis. A model demonstrating superior performance would have an AUC value approaching 1, signifying the model's strong separability or, in other words, its robust ability to accurately distinguish between positive (damage exists) and negative (no damage) instances.

It is noteworthy that both our model and the benchmark methods output probability estimates of hazards or impacts. For the purpose of this paper, we apply a threshold to our probability estimates to classify them into "damage exists" and "no damage" categories. The application of the threshold facilitates a more tangible and practical comparison of our model's performance. Moreover, the ROC curve is instrumental in visualizing how the performance of our model fluctuates under varying thresholds, ranging between 0 and 1. This provides a more comprehensive and unbiased evaluation, accommodating the potential for different threshold values in different real-world scenarios.

4.5. Benchmarks

We consider three types of benchmark methods—optical imagery-based models that are commonly utilized to estimate building damage from optical satellite imagery, fragility curve-based models that leverage empirical experiments to learn structural fragility functions and are commonly utilized in civil engineering, as well as pure DPM-based model that directly estimate building damage from InSAR imagery, especially Damage Proxy Maps. These three types of baselines help thoroughly compare the performance of our framework compared to traditional post-hurricane building damage detection methods.

4.5.1. Optical imagery-based baselines

We utilize high-resolution optical satellite imagery and associated state-of-the-art models as baselines. The dataset is described in Appendix. We select two models from top-5 winning solutions of the xView2 Computer Vision for Building Damage Assessment Challenge[5] as our benchmark. The first model (FCS-Net [29]) introduces a Siamese architecture including two encoders and one decoder. We evaluate our data by selecting the ResNet34 [25] as the encoder and the U-Net [24] as the decoder. The second model (Dual-HRNet[6]) presents a network architecture, which includes two HRNet [73,74] and several fusion blocks. To better evaluate the performance of benchmark models, we first test the pre-trained models using both our training and test datasets, without any fine-tuning. Subsequently, we finetune the pre-trained models using our training set, and gauge the performance of the finetuned model by testing it on our test set. The results of the benchmark models with and without finetuning are shown in Table 1.

---

[5] https://www.xview2.org/
[6] https://github.com/DIUx-xView/xView2_fifth_place/blob/master/figures/xView2_White_Paper_SI_Analytics.pdf

Table 1

Comparison of TPR, TNR, and AUC of our model and baselines. Note that (1) our probabilistic model that fuses DPMs and physics-based flood and wind model does not require any labels in training stage, (2) FCS-Net and Dual-HRNet are computer vision models using optical satellite imagery and pretrained in historical events. "w/o finetuning" means the model is directly adopted to estimate building damage, which is equivalent to our model setup, "finetuned" means the model is finetuned using labeled building damage datasets for Hurricane Ian. The results show that our model that does not require any labeled data achieves comparable performance as the model finetuned on labeled data. NA means Not Available, meaning AUC is not calculated for deterministic model like FCS-Net and Dual-HRNet.

Model	TPR	TNR	AUC
Our model (w/o label training)	**0.8293**	**0.6221**	**0.7553**
FCS-Net (w/o finetuning)	0.2713	0.8941	NA
FCS-Net (w/ finetuning)	0.2098	0.9386	NA
Dual-HRNet (w/o finetuning)	0.0912	0.9795	NA
Dual-HRNet (w/ finetuning)	0.8217	0.6251	NA
DPM-based Model (w/o label training)	0.6498	0.6249	0.6739
Fragility Curve (w/o label training)	0.5669	0.6246	0.5695

4.5.2. Fragility curves

In our analysis, we have utilized a fragility curve developed by Andres Paleo-Torres and his team [64], focused on Florida's residential structures and their vulnerability to hurricane-induced coastal flooding. The team's methodology transformed tsunami fragility functions into coastal flood fragility functions. They defined six damage states for commonly found 1 to 3-story reinforced concrete and timber residential buildings in Florida. This method, still under FEMA/USACE, sought to adapt a comprehensive set of tsunami-related building fragility functions. This approach draws significantly from the work of the FEMA/USACE. The result is an engineering model that generates building vulnerability functions, estimating the average building damage ratio relative to hazard intensity, specifically inundation height relative to ground level for coastal floods. Essentially, the building damage ratio represents the cost of repairing a damaged building versus its replacement value. It is crucial to note that the study's focus on Florida and its prevalent residential structures makes the resulting fragility curve a fitting benchmark for us. This tool allows for an accurate assessment of the vulnerability of similar structures in Florida to hurricane-induced coastal flooding, providing a robust basis for our further analysis and insights.

4.6. Results

In this section, we present the results derived from our model and draw comparisons with conventional methodologies, including the flood-map-based model, DPM-based model, and optical imagery-based models. This comparative analysis offers a clear understanding of our model's performance, highlighting its advantages and potential improvements over traditional techniques.

4.6.1. Result analysis

Our results conclusively demonstrate that our model, trained without the necessity for labels, exhibits a competitive edge when compared to models trained through traditional means. Regarding the True Positive Rate (TPR), our model achieved a score of 0.8293, outpacing all other models in the comparison. For the True Negative Rate (TNR), it posted a score of 0.6221. Despite this score not being the highest TNR, it remains a commendable result in comparison to the other models. Our model also led the pack with the highest Area Under the Curve (AUC) score at 0.7553 amongst all models boasting a valid AUC score.

Our model's performance was on par with the Dual-HRNet model with fine-tuning, a model that necessitates labels for training. The fine-tuned Dual-HRNet model's TPR and TNR scores of 0.8217 and 0.6251, respectively, are slightly lower and marginally higher than our model's, underscoring its competitive performance despite foregoing the use of labels.

Furthermore, the Pure DPM-based Estimation yielded a TPR of 0.6498 and a TNR of 0.6249. Likewise, the Fragility Curve-based Estimation model returned a TPR of 0.6969 and a TNR of 0.5552, with both scores trailing ours. It is notable that our pure dpm-based method is built without the flood or wind map, which shows the importance of the flood and wind map used in our model. Moreover, our model's independence from ground truth labels, is often a significant impediment due to the time and resources required to label data accurately. By discarding this requirement, our model simplifies the training process and economizes resources.

In conclusion, the evidence supports the potential of our model. It not only eliminates the need for labels, paving the way for more efficient model training, but it also holds its own against models trained via traditional, label-dependent methods. Consequently, our model emerges as a promising contender in situations where procuring ground truth labels proves challenging or impracticable.

4.6.2. Ablation study

To further understand the contributions of various components and parameters in our model, we conducted an ablation study, focusing specifically on batch size and the incorporation of Variational Inference (VI) and Pruning strategies.

Initially, we examined the influence of batch size on our model's computational time and performance, with performance measured by the Area Under the Curve (AUC). As shown in Table 2, a distinct pattern emerges: an increase in batch size leads to a reduction in computational time. To be specific, a batch size of 128 resulted in the longest computational time of 5812 s, while a four-fold increase to a batch size of 1024 reduced the computation time significantly to 941 s.

Table 2
The computational time for different batch sizes.

Batch size m	128	256	512	1024
AUC	0.7553	0.7553	0.7329	0.7311
Time used (s)	5812	2729	1267	941

Table 3
Evaluation of the effectiveness of Variational Inference and Pruning strategy in our framework. We present AUC values and variational lower bound (VLB).

Method	AUC	VLB
VI Full	0.7825	1.1442
VI Local	0.7553	1.1249
MCMC Full	0.7271	0.7797
MCMC Local	0.7117	0.7140

Nevertheless, this decrease in computational time appeared to incur a marginal decline in performance. For batch sizes of 128 and 256, the model's AUC remained steady at 0.7553, but dropped to 0.7329 and 0.7311 for batch sizes of 512 and 1024 respectively. This indicates a trade-off between computational efficiency and model performance, suggesting that the optimal batch size would depend on the specific balance between computational constraints and performance requirements in any given scenario.

In the second phase of our ablation study, we assessed the impact of Variational Inference and Pruning strategies. As seen in Table 3, we compared the performance (as gauged by AUC) and Variational Lower Bound (VLB) of four approaches: VI Full, VI Local, MCMC Full, and MCMC Local. In terms of VI Local, it refers to Local Graph Pruning, a technique — we introduced local graph pruning in Section 3. On the other hand, VI Full signifies the inference of posteriors using the complete graph. Both MCMC Local and MCMC Full refer to the same concept, namely the application of Markov Chain Monte Carlo (MCMC) with either a Local Pruned Graph or a Full Graph. The VI Full method recorded an AUC of 0.7825 and a VLB of 1.1442. In contrast, the MCMC Local method yielded the least favorable results, with an AUC of 0.7117 and a VLB of 0.7140. This comparison clearly highlights the superior performance of Variational Inference methods (both Full and Local) over MCMC methods in terms of AUC and VLB, thereby confirming their value within our framework. Additionally, a comparison within both VI and MCMC methods reveals that although the Local Pruned Graph leads to a slight decrease in AUC compared to the Full graph, the VLB is lower. This finding suggests that the Local Pruned Graph can deliver a tighter lower bound at the minor expense of AUC.

In summary, this ablation study provides critical insights into how varying components and parameters within our model influence its performance and efficiency. It underscores the impact of batch size on computational time, substantiates the superior performance of Variational Inference methods, and establishes the value of our Local Pruned Graph within our framework.

5. Discussion and conclusion

This paper proposed a novel deep learning model based on the causal Bayesian network to rapidly assess post-hurricane building damage from InSAR imagery data. By using Hurricane Ian as a case study, our model can significantly outperform the state-of-the-art benchmarks trained on the optical imagery data as well as the traditional fragility curve-based estimation. Particularly, our model does not require any ground truth labels of the impacted buildings for training or prediction, which can be readily deployed within days of the landfall.

The main reason for the superior performance of our model lies in the nature of the causal graph to best approximate the real physical processes of a hurricane triggering multiple secondary hazards and finally jointly resulting in building damage. Compared to previous models that focus on learning mapping relationships from highly noisy remote sensing observations to building damage, the causal Bayesian network considers various causes of building damage (flood, wind) as well as causes of signal changes in remote sensing observations (flood and building damage). Moreover, this approach enables effective integration of physics-based flood and wind estimates with remote sensing observations, which finally yields more accurate and timely estimation.

Moreover, the poor performance of the optical imagery benchmarks (FCS-Net and Dual-HRNet) is mainly due to the lack of model generalizability for new events (i.e., the negative transfer issues [10]) and the limitations of the data. Ideally, these benchmarks trained on a large sample from many different historical events were expected to perform well for the Hurricane Ian case study, but the results showed quite the opposite: Without finetuning, FCS-Net and Dual-HRNet had extremely low TPR (Table 1), which reflected these models' limited capabilities to make good predictions for new events. Additionally, with finetuning, FCS-Net still performed poorly while Dual-HRNet had a significant improvement in terms of TPR. However, finetuning these models is not a trivial task, which requires pre- and post-event imageries from the same region and the ground truth labels of the impacted buildings. Particularly, collecting and annotating the ground truth is time-consuming and requires domain expertise.

Admittedly, our model only considers identifying the binary damage level (i.e., damaged vs. no damage) for each building, since distinguishing different damages (e.g., a small crack of wall vs. structural damage) from satellite images (where we can usually only see roofs), and even from field investigations, is challenging. Future works may consider using more detailed damage-level identifications to better facilitate the hurricane emergency responses and community recovery process.

In conclusion, our research presents a novel causal Bayesian network model that significantly improves post-hurricane building damage assessment, as evidenced in our Hurricane Ian case study. This work, for the first time, shows that the causal dependency informed by physical understandings of hurricane-damaging processes makes it possible to connect and integrate multi-modal multi-sourced data representing different elements in these processes, in a physically interpretable way. Therefore, integrating causal dependencies modeling is beneficial to help mitigate the impacts of noises and uncertainties of the data on damage assessment accuracy. The study highlights the shortcomings of relying solely on optical imagery for assessing the impact of Hurricane Ian. It emphasizes the need for models that can adapt to new and varying situations, and points out the difficulties in depending solely on optical imagery can be significantly influenced by environmental conditions.

While our model marks a substantial step forward, we acknowledge its limitations in areas with steep slopes and water bodies affecting SAR backscatter. This insight directs our future work towards multi-modal multi-sourced data fusion, including InSAR data, optical imagery data, social media posts, news, and hurricane characteristics approximated by physical models, to further refine the model's accuracy and applicability across diverse disaster-related information [75,76]. The advancements and lessons gleaned from this research pave the way for more robust, efficient, and versatile tools in the field of disaster management and recovery.

CRediT authorship contribution statement

Chenguang Wang: Data curation, Formal analysis, Resources, Visualization, Writing – original draft, Writing – review & editing. **Yepeng Liu:** Software, Writing – original draft, Writing – review & editing. **Xiaojian Zhang:** Conceptualization, Formal analysis, Funding acquisition, Methodology, Project administration, Software, Writing – original draft, Writing – review & editing, Investigation. **Xuechun Li:** Formal analysis, Methodology, Resources, Supervision, Writing – original draft, Writing – review & editing. **Vladimir Paramygin:** Data curation, Resources. **Peter Sheng:** Data curation, Resources. **Xilei Zhao:** Formal analysis, Resources, Supervision, Writing – original draft, Writing – review & editing. **Susu Xu:** Data curation, Methodology, Supervision, Writing – original draft, Writing – review & editing, Formal analysis, Funding acquisition, Resources, Software.

Declaration of competing interest

Data availability

The authors do not have permission to share data.

Acknowledgments

Appendix

Optical Imagery Dataset Preparation: We create two datasets, including both the pre-hurricane (01/21/2022) and post-hurricane (09/30/2022) remote sensing images of most regions of Lee County, FL, to align with the requirements of the selected baseline models. The remote sensing images (GeoTIFF file) were downloaded from Maxar [77]. We partitioned the whole GeoTIFF file into small patches (1024 pixels × 1024 pixels) and identified the geo-location of each damage level-labeled parcel within each patch. This process finally yields 62 patches. An example of the remote sensing image patch (part of the left-bottom area shown in Fig. 2(b)) from both pre-hurricane and post-hurricane is shown in Fig. 4. We split 50 patches for fine-tuning the baseline models and used 12 patches for testing purposes. In total, 905 (36.6%) parcels are covered by both pre-hurricane and post-hurricane remote sensing images. For the training dataset, 636 buildings were included, in which the numbers of no-damage, minor-damage (note that we combine both minor and moderate damage into one category here to keep consistency with the baseline model), major-damage,
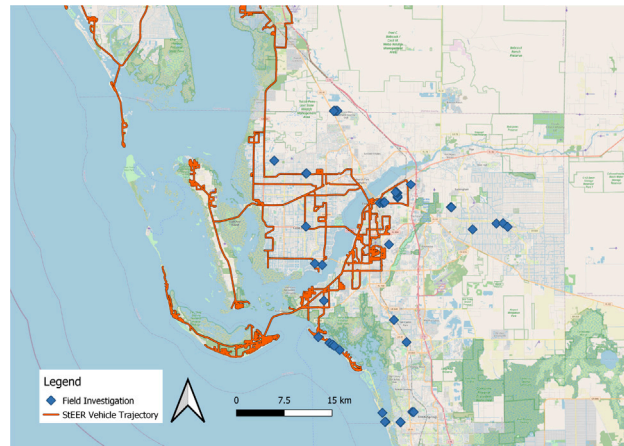
Fig. 5. Trajectory of StEER vehicles [4] and field investigation places.

Table 4
Damage level annotation across evacuation zones.

Evacuation zone	Damage level					
	0 No damage	1 Minor damage	2 Moderate damage	3 Major damage	4 Destroyed	In total
A	1049	167	165	79	30	1490
B	227	23	15	2	0	299
C	204	33	22	1	0	267
D	178	61	36	24	0	260
E	17	1	3	4	0	25
Non-evacuation	110	7	3	9	2	131
In total	1785	292	244	119	32	2472
	No damage: 1785 (72.2%)			Damaged: 687 (27.8%)		

and destroyed buildings are 576, 34, 21, and 5 separately. For the test dataset, 269 buildings were included, in which the numbers of no-damage, minor-damage, major-damage, and destroyed buildings are 195, 32, 30, and 12, respectively.

Ground truth data collection details: Specifically, StEER sent several vehicles equipped with panoramic cameras to collect near real-time street views of buildings, streets and other infrastructures in order to get a rapid response to Hurricane Ian damage assessment [66,78]. We can access all static street-view images at any available location provided by StEER. We took the following steps to gather data from StEER. First, we retrieved parcel footprint data from Lee County GIS Open Data Portal (https://maps.leegov.com/pages/data). We further collected the trajectory of StEER's panoramic vehicles, as shown in Fig. 5. We created a 10-meter buffer for all trajectories and spatially intersected it with parcel footprints to identify all potentially viewable buildings. Three groups of annotators (group size equals to two) were deployed to manually screenshot images of buildings from Hurricane Ian Street View Comparison interactive website [4], focusing on the viewable buildings. Each building's exact address and a couple of characteristics (e.g., building type and value) were also recorded. Three representative regions in Evacuation Zone A that were highly impacted by the storm, i.e., Sanibel, Fort Myers beach and inland coastal areas, were assigned to three groups, respectively.

We note that most of the images collected by StEER are within Evacuation Zone A. Therefore, to prepare a more comprehensive dataset for training the models, additional field investigation data for the damaged structures that do not have adequate street-view images or are missing from the existing StEER database (e.g., from other evacuation zones) are required. We deployed four people to manually gather additional imagery data in Lee County, FL. This field investigation group used smartphones for recording street views. Building images from the collected videos were manually screenshotted afterward. Places of field investigation data collection are shown in Fig. 5.

Wind Map and Flood Map Acquisition: To optimize the use of the wind data, we initially construct a dot wind map, then employ interpolation methods to convert the discrete data points into a comprehensive, continuous wind map, as shown in Fig. 3. This map is carefully aligned with the grid and resolution of the Damage Proxy Map (DPM) for seamless integration. Ultimately, these refined datasets will be incorporated into our predictive model. In doing so, we aim to enhance our understanding of these severe weather events, enabling us to predict their paths and potential impacts more accurately. This will, in turn, better equip us to manage and mitigate the effects of such events on our environment and communities.

The Flood map is based on the simulation of a coupled storm surge-wave modeling system CH3D-SWAN [69] using boundary-fitted grids with a minimum grid size of 20 meters for the Charlotte, Lee, and Collier Counties of Florida. The model was forced

Table 5

Damage States and Extent of Failure From Field assessment structural team (FAST) Handbook [67].

Damage state	Short description	Roof or wall cover	Window or door	Roof or wall substr.	Roof struct.	Wall struct.
0	No visible damage or very minor damage	0%	No	No	No	No
1	Minor damage Damage confined to envelope	>2% and ≤15%	1	No	No	No
2	Moderate damage Load path preserved, but significant repairs required	>15% and <50%	>1 and ≤the larger of 3 and 20%	1 to 3 panels	No	No
3	Severe Damage Major impacts to structural load path	>50%	>the larger of 3 and 20% and ≤50%	>3 and ≤25%	≤15%	No
4	Destroyed Total loss. Structural load path compromised beyond repair.	>50%	>50%	>25%	>15%	Yes

Table 6

Comparison of True Positive Rate Results with different damaged classification settings.

Our model	True Positive Rate
0 vs 1,2,3,4	0.69589
0,1 vs 2,3,4	0.78595
0,1,2 vs 3,4	0.82418
0,1,2,3 vs 4	0.80556

by a hurricane wind model for Ian [70] with offshore water level simulated by a large-scale surge and tide model. Simulated water levels agree well with observed surge level and High Water Marks (HWMs) at nearly 100 locations.

The Flood Map can be conceptualized similarly to the Damage Proxy Map, as shown in Fig. 3. In this case, it portrays the surge's flood elevation as a composition of small blocks, each representing a particular value under the grid system. This approach allows the Flood map to precisely depict post-hurricane flood elevation patterns, trends, and distributions.

To integrate the Flood map into our analysis, we align it with the fine grid system used in the Damage Proxy Map. This re-projection process is straightforward and facilitates a seamless integration of the Flood map into both the fragility calculator and our model computations.

Damage Level Setting: In our investigation, we initially utilized damage classifications from the FAST Handbook [67] by the StEER Network for the field investigation, as detailed in Table 5, to establish a consistent framework from field assessments. Recognizing that the original classification was complex for the scope of our current work, we simplified the approach to classify the building damage level. The result of different damage level settings was documented in Table 6, where we evaluated various damage class configurations against TPR outcomes. We iteratively adjusted our classification schema, starting from a "0 vs 1,2,3,4" comparison and evolving to a "0,1 vs 2,3,4" scenario, to understand the TPR dynamics better. Our analysis led us to adopt a "0,1,2 vs 3,4" configuration as the optimal setting for TPR, which streamlined the categorization into a binary state of 'No damage' for levels 0 to 2 and 'Damaged' for levels 3 and 4. This standard not only corresponds to the realities of fieldwork—where visually discerning minor damage levels can be challenging—but also accounts for the constraints of satellite imagery, which cannot detect finer details such as wall cracks from space. Moreover, it establishes an objective for future research aimed at enhancing the precision of building damage detection.

References

[1] A. Smith, US billion-dollar weather and climate disasters in historical context (NOAA national centers for environmental information), 2021.

[2] Wei Zhai, Zhong-Ren Peng, Damage assessment using Google street view: Evidence from Hurricane Michael in Mexico beach, Florida, Appl. Geogr. 123 (2020) 102252.

[3] Polina Berezina, Desheng Liu, Hurricane damage assessment using coupled convolutional neural networks: A case study of Hurricane Michael, Geomat. Nat. Hazards Risk 13 (1) (2022) 414–431.

[4] Structural Extreme Events Reconnaissance (StEER), Hurricane Ian street view comparison, 2023, Available online (Accessed on 20 June 2023).

[5] Hassan Masoomi, John W. van de Lindt, Mohammad R. Ameri, Trung Q. Do, Bret M. Webb, Combined wind-wave-surge Hurricane-induced damage prediction for buildings, J. Struct. Eng. 145 (1) (2019) 04018227.

[6] Susu Xu, Hae Young Noh, PhyMDAN: Physics-informed knowledge transfer between buildings for seismic damage diagnosis through adversarial learning, Mech. Syst. Signal Process. 151 (2021) 107374.

[7] Susu Xu, Hae Young Noh, Knowledge transfer between buildings for seismic damage diagnosis through adversarial learning, 2020, arXiv preprint arXiv:2002.09513.

[8] Chen Lin, Yundong Li, Yi Liu, Xiang Wang, Shuo Geng, Building damage assessment from post-hurricane imageries using unsupervised domain adaptation with enhanced feature discrimination, IEEE Trans. Geosci. Remote Sens. 60 (2021) 1–10.

[9] Landon Calton, Zhangping Wei, Using artificial neural network models to assess Hurricane damage through transfer learning, Appl. Sci. 12 (3) (2022) 1466.

[10] Hao Wang, Chao Tao, Ji Qi, Rong Xiao, Haifeng Li, Avoiding negative transfer for semantic segmentation of remote sensing images, IEEE Trans. Geosci. Remote Sens. 60 (2022) 1–15.

[11] John A. Barras, Satellite Images and Aerial Photographs of the Effects of Hurricanes Katrina and Rita on Coastal Louisiana, Technical Report, Geological Survey (US), 2007.

[12] Susu Xu, Joshua Dimasaka, David J. Wald, Hae Young Noh, Seismic multi-hazard and impact estimation via causal inference from satellite imagery, Nature Commun. 13 (1) (2022) 7793.

[13] Saro Lee, Application of logistic regression model and its validation for landslide susceptibility mapping using GIS and remote sensing data, Int. J. Remote Sens. 26 (7) (2005) 1477–1491.

[14] Chaoying Zhao, Zhong Lu, Remote sensing of landslides—A review, Remote Sens. 10 (2) (2018) 279.

[15] Asim Bashir Khajwal, Chih-Shen Cheng, Arash Noshadravan, Multi-view deep learning for reliable post-disaster damage classification, 2022, arXiv: 2208.03419.

[16] Xiao Liang, Image-based post-disaster inspection of reinforced concrete bridge systems using deep learning with Bayesian optimization, Comput.-Aided Civ. Infrastruct. Eng. 34 (2018) 415–430.

[17] Wei Zhai, Zhong-Ren Peng, Damage assessment using Google street view: Evidence from Hurricane Michael in Mexico beach, Florida, Appl. Geogr. (ISSN: 0143-6228) 123 (2020) 102252, http://dx.doi.org/10.1016/j.apgeog.2020.102252.

[18] Chen Feng, Ming-Yu Liu, Chieh-Chi Kao, Teng-Yok Lee, Deep active learning for civil infrastructure defect detection and classification, in: Computing in Civil Engineering 2017, 2017, pp. 298–306, http://dx.doi.org/10.1061/9780784480823.036.

[19] Yuqing Gao, Khalid Mosalam, Deep transfer learning for image-based structural damage recognition, Comput.-Aided Civ. Infrastruct. Eng. 33 (2018) http://dx.doi.org/10.1111/mice.12363.

[20] Haiyan Hao, Yan Wang, Hurricane damage assessment with multi-, crowd-sourced image data: A case study of Hurricane irma in the city of Miami, in: Proceedings of the 17th International Conference on Information System for Crisis Response and Management, ISCRAM, Valencia, Spain, 2019, pp. 19–22.

[21] Quoc Dung Cao, Youngjun Choe, Building damage annotation on post-hurricane satellite imagery based on convolutional neural networks, Nat. Hazards 103 (3) (2020) 3357–3376, http://dx.doi.org/10.1007/s11069-020-04133-2.

[22] Chih-Shen Cheng, Amir H. Behzadan, Arash Noshadravan, Deep learning for post-hurricane aerial damage assessment of buildings, Comput.-Aided Civ. Infrastruct. Eng. 36 (6) (2021) 695–710.

[23] Quoc Dung Cao, Youngjun Choe, Post-hurricane damage assessment using satellite imagery and geolocation features, 2020, arXiv preprint arXiv:2012.08624.

[24] Olaf Ronneberger, Philipp Fischer, Thomas Brox, U-Net: Convolutional networks for biomedical image segmentation, 2015, arXiv:1505.04597.

[25] Kaiming He, Xiangyu Zhang, Shaoqing Ren, Jian Sun, Deep residual learning for image recognition, 2015, arXiv:1512.03385.

[26] Andrew G. Howard, Menglong Zhu, Bo Chen, Dmitry Kalenichenko, Weijun Wang, Tobias Weyand, Marco Andreetto, Hartwig Adam, MobileNets: Efficient convolutional neural networks for mobile vision applications, 2017, arXiv:1704.04861.

[27] Mingxing Tan, Quoc V. Le, EfficientNet: Rethinking model scaling for convolutional neural networks, 2020, arXiv:1905.11946.

[28] Ritwik Gupta, Richard Hosfelt, Sandra Sajeev, Nirav Patel, Bryce Goodman, Jigar Doshi, Eric Heim, Howie Choset, Matthew Gaston, xBD: A dataset for assessing building damage from satellite imagery, 2019, arXiv:1911.09296.

[29] Eugene Khvedchenya, Tatiana Gabruseva, Fully convolutional siamese neural networks for buildings damage assessment from satellite images, 2021, arXiv:2111.00508.

[30] Ethan Weber, Hassan Kané, Building disaster damage assessment in satellite imagery with multi-temporal fusion, 2020, arXiv:2004.05525.

[31] Xuechun Li, Paula M Bürgi, Wei Ma, Hae Young Noh, David Jay Wald, Susu Xu, Disasternet: Causal Bayesian networks with normalizing flows for cascading hazards estimation from satellite imagery, in: Proceedings of the 29th ACM SIGKDD Conference on Knowledge Discovery and Data Mining, 2023, pp. 4391–4403.

[32] Xuechun Li, Paula M Burgi, Wei Ma, Hae Young Noh, David J Wald, Susu Xu, Normalizing flow-based deep variational Bayesian network for seismic multi-hazards and impacts estimation from InSAR imagery, 2023, arXiv preprint arXiv:2310.13805.

[33] Chenguang Wang, Yepeng Liu, Xiaojian Zhang, Xuechun Li, Vladimir Paramygin, Arthriya Subgranon, Peter Sheng, Xilei Zhao, Susu Xu, Causality-informed rapid post-hurricane building damage detection in large scale from InSAR imagery, in: Proceedings of the 8th ACM SIGSPATIAL International Workshop on Security Response using GIS, 2023, pp. 7–12.

[34] Susu Xu, Joshua Dimasaka, David J Wald, Hae Young Noh, Bayesian updating of seismic ground failure estimates via causal graphical models and satellite imagery, 2022, arXiv preprint arXiv:2204.07653.

[35] Kristy F. Tiampo, Lingcao Huang, Conor Simmons, Clay Woods, Margaret T. Glasscoe, Detection of flood extent using sentinel-1A/B synthetic aperture radar: An application for Hurricane Harvey, Houston, TX, Remote Sens. 14 (9) (2022) 2261.

[36] Yunung Nina Lin, Sang-Ho Yun, Alok Bhardwaj, Emma M. Hill, Urban flood detection with sentinel-1 multi-temporal Synthetic Aperture Radar (SAR) observations in a Bayesian framework: A case study for Hurricane Matthew, Remote Sens. 11 (15) (2019) 1778.

[37] Susu Xu, Joshua Dimasaka, David J Wald, Hae Young Noh, Fusing damage proxy maps with geospatial models for Bayesian updating of seismic ground failure estimations: A case study in central italy, in: EGU General Assembly Conference Abstracts, 2021, pp. EGU21–13619.

[38] Peter J. Vickery, Peter F. Skerlj, Jason Lin, Lawrence A. Twisdale Jr., Michael A. Young, Francis M. Lavelle, HAZUS-MH Hurricane model methodology. II: Damage and loss estimation, Nat. Hazards Rev. 7 (2) (2006) 94–103.

[39] Tori Tomiczek, Andrew Kennedy, Yao Zhang, Margaret Owensby, Mark E. Hope, Ning Lin, Abigail Flory, Hurricane damage classification methodology and fragility functions derived from Hurricane Sandy's effects in coastal New Jersey, J. Waterw. Port Coast. Ocean Eng. 143 (5) (2017) 04017027.

[40] Ahmed U. Abdelhady, Seymour M.J. Spence, Jason McCormick, Risk and fragility assessment of residential wooden buildings subject to Hurricane winds, Struct. Saf. 94 (2022) 102137.

[41] Leonardo A Sierra, Víctor Yepes, Tatiana García-Segura, Eugenio Pellicer, Bayesian network method for decision-making about the social sustainability of infrastructure projects, J. Cleaner Product. 176 (2018) 521–534.

[42] Ke Li, Shizhe Li, Ruwen Qin, Development of a causal model for improving rural seniors' accessibility: Data evidences, 2024, arXiv preprint arXiv: 2401.13107.

[43] Iris Tien, Armen Der Kiureghian, Algorithms for Bayesian network modeling and reliability assessment of infrastructure systems, Reliab. Eng. Syst. Safety 156 (2016) 134–147.

[44] Susu Xu, Xuechun Li, Haeyoung Noh, David J Wald, Deep causal Bayesian network for modeling spatial seismic building damage from remote sensing observations, in: AGU Fall Meeting Abstracts, 2022, 2022, INV44A–02.

[45] Md Tanjin Amin, Faisal Khan, Salim Ahmed, Syed Imtiaz, A novel data-driven methodology for fault detection and dynamic risk assessment, Can. J. Chem. Eng. 98 (11) (2020) 2397–2416.

[46] James Daley, Faisal Khan, Md Tanjin Amin, Process safety analysis using operational data and Bayesian network, Process Saf. Prog. 42 (2) (2023) 269–280.

[47] Shangjia Dong, Tianbo Yu, Hamed Farahmand, Ali Mostafavi, Probabilistic modeling of cascading failure risk in interdependent channel and road networks in urban flooding, Sustainable Cities Soc. 62 (2020) 102398.

[48] Hongjun Joo, Changhyun Choi, Jungwook Kim, Deokhwan Kim, Soojun Kim, Hung Soo Kim, A Bayesian network-based integrated for flood risk assessment (InFRA), Sustainability 11 (13) (2019) 3733.

[49] Peiwei Xin, Faisal Khan, Salim Ahmed, Dynamic hazard identification and scenario mapping using Bayesian network, Process Saf. Environ. Prot. 105 (2017) 143–155.

[50] Zening Wu, Yanxia Shen, Huiliang Wang, Meimei Wu, Assessing urban flood disaster risk using Bayesian network model and GIS applications, Geomat. Nat. Hazards Risk 10 (1) (2019) 2163–2184.

[51] Weiyi Chen, Limao Zhang, Predicting building damages in mega-disasters under uncertainty: An improved Bayesian network learning approach, Sustainable Cities Soc. 66 (2021) 102689.

[52] Yee Kit Chan, Voon Koo, An introduction to Synthetic Aperture Radar (SAR), Prog. Electromagn. Res. B 2 (2008) 27–60.

[53] Sang-Ho Yun, Eric Fielding, Mark Simons, Piyush Agram, Paul Rosen, Susan Owen, Frank Webb, Rapid and reliable damage proxy map from InSAR coherence, in: IEEE GeoScience and Remote Sensing Society, IGARSS 2012, 2012.

[54] National Institute of Standards and Technology and Applied Research Associates, NIST-ARA Windfield Data Release 3, 2022, Accessed: [Insert Date Here], https://www.designsafe-ci.org/data/browser/public/designsafe.storage.community/Recon%20Portal/2022%20Hurricane%20Ian/NIST-ARA%20Windfield%20Data%20Release%203.

[55] Y. Peter Sheng, Vladimir A. Paramygin, Adail A. Rivera-Nieves, Ruizhi Zou, Sarah Fernald, Timothy Hall, Klaus Jacob, Coastal marshes provide valuable protection for coastal communities from storm-induced wave, flood, and structural loss in a changing climate, Sci. Rep. 12 (1) (2022) 3051.

[56] Ryan Paulik, Alec Wild, Conrad Zorn, Liam Wotherspoon, Residential building flood damage: Insights on processes and implications for risk assessments, J. Flood Risk Manag. 15 (4) (2022) e12832.

[57] Chaochao Li, Xiaotao Cheng, Na Li, Xiaohe Du, Qian Yu, Guangyuan Kan, A framework for flood risk analysis and benefit assessment of flood control measures in urban areas, Int. J. Environ. Res. Public Health 13 (8) (2016) 787.

[58] Carol J. Friedland, Melanie Gall, True cost of Hurricanes: Case for a comprehensive understanding of multihazard building damage, Leadersh. Manag. Eng. 12 (3) (2012) 134–146.

[59] J.-P. Pinelli, G. Pita, K. Gurley, B. Torkian, S. Hamid, C. Subramanian, Damage characterization: Application to Florida public Hurricane loss model, Nat. Hazards Rev. 12 (4) (2011) 190–195.

[60] Joseph Wartman, Jeffrey W. Berman, Ann Bostrom, Scott Miles, Michael Olsen, Kurtis Gurley, Jennifer Irish, Laura Lowes, Troy Tanner, Jake Dafni, et al., Research needs, challenges, and strategic approaches for natural hazards and disaster reconnaissance, Front. Built Environ. (2020) 182.

[61] Yuting Lu, Penghai Wu, Xiaoshuang Ma, Xinghua Li, Detection and prediction of land use/land cover change using spatiotemporal data fusion and the cellular automata–Markov model, Environ. Monit. Assess. 191 (2019) 1–19.

[62] Omimah Alsaadi, Emrah Acar, Challenges of post-disaster reconstruction projects: An empirical investigation according to project management knowledge areas, Am. J. Manag. 21 (4) (2021).

[63] Alican Karaer, Mingyang Chen, Michele Gazzea, Mahyar Ghorbanzadeh, Tarek Abichou, Reza Arghandeh, Eren Erman Ozguven, Remote sensing-based comparative damage assessment of historical storms and Hurricanes in Northwestern Florida, Int. J. Disaster Risk Reduct. 72 (2022) 102857.

[64] Andres Paleo-Torres, Kurtis Gurley, Jean-Paul Pinelli, Mohammad Baradaranshoraka, Mingwei Zhao, Anawat Suppasri, Xinlai Peng, Vulnerability of Florida residential structures to Hurricane induced coastal flood, Eng. Struct. 220 (2020) 111004.

[65] Tommi S. Jaakkola, Michael I. Jordan, A variational approach to Bayesian logistic regression models and their extensions, in: Sixth International Workshop on Artificial Intelligence and Statistics, PMLR, 1997, pp. 283–294.

[66] Tracy Kijewski-Correa, David Prevatt, David Roueche, Ian Robertson, Mohammad Alam, Amir Safiey, Ioannis Zisis, Oscar Lafontaine, Omar Nofal, Landolf Rhode-Barbarigos, Arthriya Subgranon, Dylan Faraone, Jonathon Micali, Jorge X Santiago-Hernández, Duzgun Agdas, StEER: Hurricane Ian Early Access Reconnaissance Report (EARR), Designsafe-CI, 2023, http://dx.doi.org/10.17603/DS2-3PC2-7P82, URL https://www.designsafe-ci.org/data/browser/public/designsafe.storage.published/PRJ-3709/#details-4421495110974640621-242ac118-0001-012.

[67] T. Kijewski-Correa, K. Mosalam, D.O. Prevatt, I. Robertson, D. Roueche, Field assessment structural team (FAST) handbook, version 1.2, 2019, Structural Engineering Extreme Events Reconnaissance.

[68] Klaus Krippendorff, Content Analysis: An Introduction to Its Methodology, Sage publications, 2018.

[69] Y. Peter Sheng, Vadim Alymov, Vladimir A. Paramygin, Simulation of storm surge, wave, currents, and inundation in the outer banks and Chesapeake Bay during Hurricane Isabel in 2003: The importance of waves, J. Geophys. Res.: Oceans 115 (C4) (2010).

[70] Y. Peter Sheng, Vladimir A. Paramygin, Kun Yang, Adail A. Rivera-Nieves, A sensitivity study of rising compound coastal inundation over large flood plains in a changing climate, Sci. Rep. 12 (1) (2022) 3403.

[71] NASA-JPL/Caltech ARIA, Damage proxy map (DPM) for Hurricane Ian using copernicus sentinel-1 data, 2022, Available at: http://aria-share.jpl.nasa.gov/.

[72] Marco Chini, Ramona Pelich, Luca Pulvirenti, Nazzareno Pierdicca, Renaud Hostache, Patrick Matgen, Sentinel-1 InSAR coherence to detect floodwater in urban areas: Houston and Hurricane Harvey as a test case, Remote Sens. 11 (2) (2019) 107.

[73] Jingdong Wang, Ke Sun, Tianheng Cheng, Borui Jiang, Chaorui Deng, Yang Zhao, Dong Liu, Yadong Mu, Mingkui Tan, Xinggang Wang, Wenyu Liu, Bin Xiao, Deep high-resolution representation learning for visual recognition, 2020, arXiv:1908.07919.

[74] Ke Sun, Yang Zhao, Borui Jiang, Tianheng Cheng, Bin Xiao, Dong Liu, Yadong Mu, Xinggang Wang, Wenyu Liu, Jingdong Wang, High-resolution representations for labeling pixels and regions, 2019, arXiv:1904.04514.

[75] Chenguang Wang, Davis Engler, Xuechun Li, James Hou, David J Wald, Kishor Jaiswal, Susu Xu, Near-real-time earthquake-induced fatality estimation using crowdsourced data and large-language models, 2023, arXiv preprint arXiv:2312.03755.

[76] James Hou, Susu Xu, Near-real-time seismic human fatality information retrieval from social media with few-shot large-language models, in: Proceedings of the 20th ACM Conference on Embedded Networked Sensor Systems, 2022, pp. 1141–1147.

[77] Maxar Technologies, Hurricane Ian, 2023, https://www.maxar.com/open-data/hurricane-ian. (Accessed: 01 May 2023).

[78] Maria Cortes, Prateek Arora, Luis Ceferino, Haitham Ibrahim, Denis Istrati, Dorothy Reed, David Roueche, Amir Safiey, Tori Tomiczek, Ioannis Zisis, Mohammad Alam, Tracy Kijewski-Correa, David Prevatt, Ian Robertson, StEER: Hurricane Ian Preliminary Virtual Reconnaissance Report (PVRR), Designsafe-CI, 2022, http://dx.doi.org/10.17603/DS2-KC9K-S242.